Supplementary Material
Linear control on nonlinear thermoacoustic instabilities with flame dynamics modeled by a level-set method

Xiaoling Chen[a], Santosh Hemchandra[b], Hosam Fathy[c], Jacqueline O'Connor[a,*]

[a] The Pennsylvania State University, University Park, PA 16802, USA
[b] Indian Institute of Science, Bengaluru, KA 560012, India
[c] University of Maryland, College Park, MD 20742, USA

---

1. Galerkin projection

1.1. Basis function - shifted Legend polynomials

We approximate the normalized velocity and pressure oscillation along the Rijke tube length x as a linear combination of known basis functions – shifted Legendre polynomials $\psi_k(x)$ – weighted by unknown time-dependent coefficients $\mu_{k,u}(t)$ and $\mu_{k,p}(t)$, as shown in Eq. (1).

$$u'_n(t,x) \approx \sum_{k=1}^{N} \mu_{k,u}(t)\psi_k(x),\ p'_n(t,x) \approx \sum_{k=1}^{N} \mu_{k,p}(t)\psi_k(x) \tag{1}$$

To apply the orthonormality of Legendre polynomials over the interval [0,1], we transform the original spatial coordinate x to a non-dimensional spatial coordinate z. The coordinate conversion is as shown in Eq. (2).

$$z = \begin{cases} \dfrac{x}{b^-}, & 0 \le x \le b \\ \dfrac{L-x}{L-b^+}, & b \le x \le L \end{cases} \tag{2}$$

The basis functions are the shifted Legendre polynomials defined in the interval [0,1] and satisfy the orthonormal property. They are transformed from

---

[*] Corresponding author
Email address: `jxo22@psu.edu` (Jacqueline O'Connor)

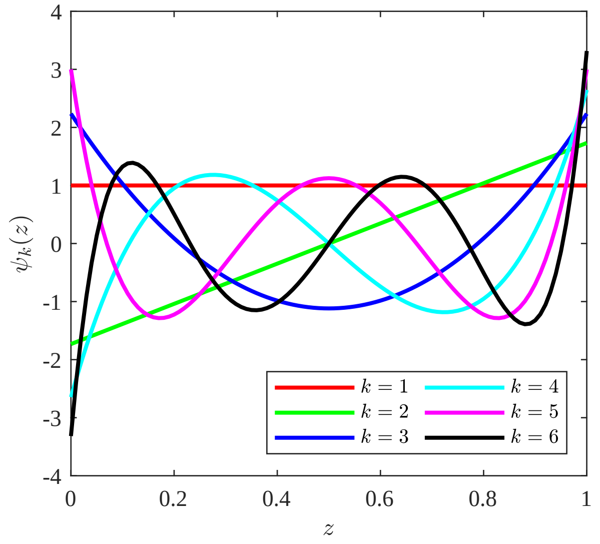

FIGURE 1. Shifted Legendre polynomials with degrees from 1 to 6

the original Legendre polynomials $P_k(z)$, which are defined in [-1,1]. The transformation is in Eq. (3). The plots of the shifted Legendre polynomials $\psi_k(z)$ with degrees from 1 to 6 are in Fig. 1.

$$\psi_k(z) = \sqrt{2k-1}P_{k-1}(k-1, 2z-1), k \in \mathbb{Z}^+, z \in [0,1] \tag{3}$$

1.2. Governing equations in two regions

The governing equations with respect to the non-dimensional spatial coordinate z for the two regions upstream and downstream of the flame are summarized in Eq. (5) and Eq. (6). The boundary condition at the Rijke tube outlet will remain a pressure-release condition, whereas the boundary condition at the Rijke tube inlet will be a non-zero value $u_{n,c}(t)$ to account for the control actuator velocity input in the control design. Two more boundary conditions at the flame location are added to close the problem. The first is pressure continuity across the flame, $p'_n(x = b^-, t) = p'_n(x = b^+, t)$. The second is the related to the flame heat release rate. The heat release rate from the flame accelerates the velocity across the flame due to an expansion effect, as shown in Eq. (4), which is derived from the integration of the energy equation over the region $[b^-,b^+]$ across the flame. The summarized two additional boundary conditions are in Eq. (7).

$$0 = -\frac{\bar{\rho}\bar{c}^2 u_0}{p_{atm}} \left[u_n'(x=b^+,t) - u_n'(x=b^-,t)\right] + (\gamma-1)\frac{Q_0}{p_{atm}} Q_n' \tag{4}$$

$$\begin{gathered} \frac{\partial u_n'}{\partial t} = -\frac{p_{atm}}{\bar{\rho}_1 u_0 b^-}\frac{\partial p_n'}{\partial z}, \ \frac{\partial p_n'}{\partial t} = -\frac{\bar{\rho}_1 \bar{c}_1^2 u_0}{p_{atm} b^-}\frac{\partial u_n'}{\partial z} \\ u_n'(z=0,t) = u_{n,c}(t) \end{gathered} \tag{5}$$

$$\begin{gathered} \frac{\partial u_n'}{\partial t} = \frac{p_{atm}}{\bar{\rho}_2 u_0 (L-b^+)}\frac{\partial p_n'}{\partial z}, \ \frac{\partial p_n'}{\partial t} = \frac{\bar{\rho}_2 \bar{c}_2^2 u_0}{p_{atm}(L-b^+)}\frac{\partial u_n'}{\partial z} \\ p_n'(z=0,t) = 0 \end{gathered} \tag{6}$$

$$\begin{gathered} p_n'(z=1^-,t) = p_n'(z=1^-,t) \\ u_n'(z=1^+,t) - u_n'(z=1^-,t) = \frac{(\gamma-1)Q_0}{\bar{\rho}\bar{c}^2 u_0} Q_n'(t) \end{gathered} \tag{7}$$

1.3. Galerkin projection

Substituting the approximated acoustic velocity and pressure from Eq. (1) into the governing equations Eq. (5) and Eq. (6), we can obtain a series of ordinary differential equations that describes the dynamics of the time-dependent weights $\mu_{k,u}(t)$ and $\mu_{k,p}(t)$. Applying the orthonormality of the basis functions, we obtain ordinary differential equations in the linear state space form, where the state variables are the time-dependent weights. The summarized state equations are in Eq. (8). The subscript j denotes the number of state variable groups and $j \le N-1$. Each group of state variables contains four individual state variables $\mu^{(1)}_{j,u}(t)$, $\mu^{(1)}_{j,p}(t)$, $\mu^{(2)}_{j,u}(t)$, and $\mu^{(2)}_{j,p}(t)$. The superscript (1) and (2) represent that the state variables are for the acoustic variables in the regions upstream and downstream of the flame. The corresponding boundary conditions serve as the algebraic constraints for the state space model, described in Eq. (9).

$$\begin{aligned}
\dot{\mu}_{j,u}^{(1)}(t) &\approx -\frac{p_{atm}}{\bar{\rho}_1 u_0 b^-} \sum_{k=1}^{N} \mu_{k,p}^{(1)}(t) \int_0^1 \frac{d\psi_k(z)}{dz} \psi_j(z) dz \\
\dot{\mu}_{j,p}^{(1)}(t) &\approx -\frac{\bar{\rho}_1 \bar{c}_1^2 u_0}{p_{atm} b^-} \sum_{k=1}^{N} \mu_{k,u}^{(1)}(t) \int_0^1 \frac{d\psi_k(z)}{dz} \psi_j(z) dz \\
\dot{\mu}_{j,u}^{(2)}(t) &\approx \frac{p_{atm}}{\bar{\rho}_2 u_0 (L - b^+)} \sum_{k=1}^{N} \mu_{k,p}^{(2)}(t) \int_0^1 \frac{d\psi_k(z)}{dz} \psi_j(z) dz \\
\dot{\mu}_{j,p}^{(2)}(t) &\approx \frac{\bar{\rho}_2 \bar{c}_2^2 u_0}{p_{atm} (L - b^+)} \sum_{k=1}^{N} \mu_{k,u}^{(2)}(t) \int_0^1 \frac{d\psi_k(z)}{dz} \psi_j(z) dz
\end{aligned} \tag{8}$$

$$\begin{aligned}
&\sum_{k=1}^{N} \mu_{k,u}^{(1)}(t) \psi_k(0) \approx 0 \\
&\sum_{k=1}^{N} \mu_{k,p}^{(2)}(t) \psi_k(0) \approx 0 \\
&\sum_{k=1}^{N} \mu_{k,p}^{(1)}(t) \psi_k(1) = \sum_{k=1}^{N} \mu_{k,p}^{(2)}(t) \psi_k(1) \\
&\sum_{k=1}^{N} \mu_{k,u}^{(2)}(t) \psi_k(1) - \sum_{k=1}^{N} \mu_{k,u}^{(1)}(t) \psi_k(1) = \frac{(\gamma - 1)}{\bar{\rho} \bar{c}^2} Q'_n(t)
\end{aligned} \tag{9}$$

The number of the state variable groups is $N-1$ and the N^{th} group can be represented by the previous $N-1$ groups based on the four boundary conditions in Eq. (9). The inputs of the state space model are the acoustic velocity from actuator at Rijke tube inlet $u_{n,c}(t)$ and fluctuating heat release rate per unit area from the flame $Q'_n(t)$. The outputs of the are selected to be the velocity right upstream of the flame $u'_{n,b}(t)$ and the pressure measured at the Rijke tube inlet $p'_{n,0}(t)$. The output $u'_{n,b}(t)$ is the input to the level-set solver that determines the flame dynamics and the output $p'_{n,0}(t)$ is the feedback to the

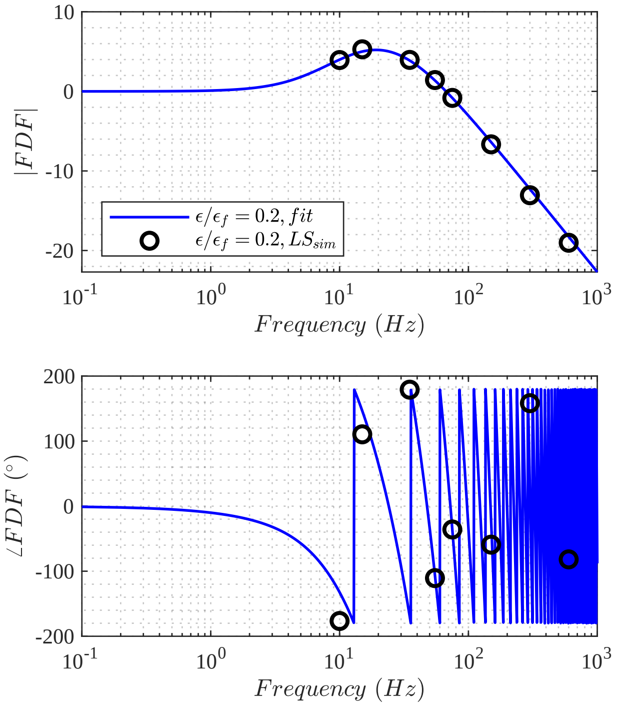

FIGURE 2. Validation of curve-fitting FDF with simulation results validation using level-set solver

controller. The state space model is written as Eq. (10).

$$\dot{\boldsymbol{x}} = A_n \boldsymbol{x} + B_n \begin{bmatrix} u_{n,c} \\ Q'_n \end{bmatrix}, \quad \begin{bmatrix} p'_{n,0} \\ u'_{n,b} \end{bmatrix} = C_n \boldsymbol{x} + D_n \begin{bmatrix} u_{n,c} \\ Q'_n \end{bmatrix} \tag{10}$$

2. FDF validation in higher frequency range

The fitted flame describing function is validated in higher frequency range using the same level-set solver. The incoming velocity only contains the axial velocity component. The comparison of the FDF in frequency domain is in Fig. 2.

The comparison shows that the curve-fitted flame describing function agrees well with the simulation results at higher frequencies up to 800 Hz, including the first four acoustic modes. The phase comparison is not as accurate as that for the magnitude, which is because that the phase information becomes less convincing when amplitude is low. Based on the comparison, the accuracy of the fitted FDF is ensured for the frequency range of interest in this paper.

3. Sensitivity of thermoacoustic model to flame location

The summary of the thermoacoustic model's characteristics in both time and frequency domain is shown in Fig.3 and Fig. 6. The velocity right upstream of the flame in the time domain is displayed in Fig.4 for all the cases. The black dashed line represent the critical velocity oscillation amplitude that causes the flame flash-back $\epsilon_f = 0.553$. Due to the property of the G-equation solver, flame base is always attached to the center-body so that either flame flashback or blowoff never happens. As a result, the flame area oscillation saturates when the velocity upstream the flame reaches the critical value ϵ_f, as shown in Fig. 5.

The mode shapes for the first four dominant acoustic mode of the pressure oscillation are in Fig. 7.

The phase difference between the oscillations of pressure at flame location and flame area is summarized in Fig. 8. The size of the scatter points in the plots represents the amplitude of the product between pressure and flame area oscillations at the mode frequencies. The size indicates the effect of the two signals. The system oscillation is dominated by the mode for which the size of the scatter points is larger.

4. Sensitivity of thermoacoustic model to temperature rise

The summary of the thermoacoustic model's characteristics in both time and frequency domain is shown in Fig.9 and Fig. 11. The corresponding flame area oscillation in the time domain is shown in Fig.10, displaying the saturation behavior within the simulation duration.

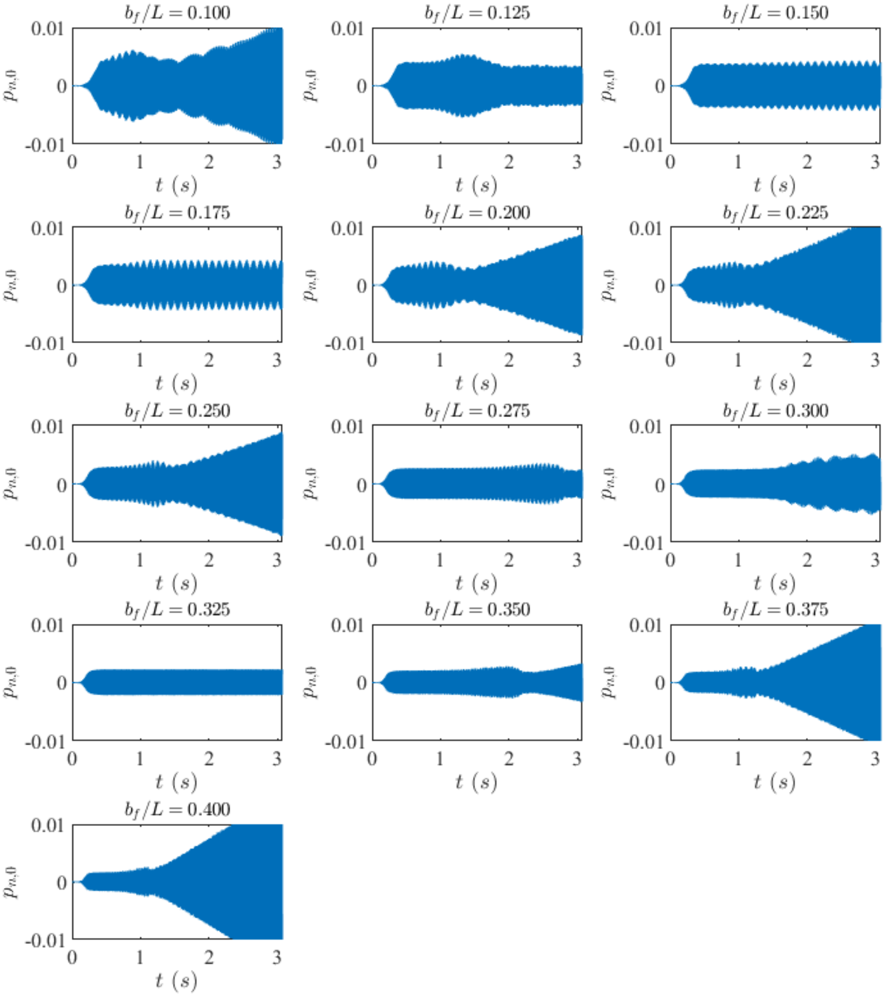

$b_f/L = 0.100$, $b_f/L = 0.125$, $b_f/L = 0.150$, $b_f/L = 0.175$, $b_f/L = 0.200$, $b_f/L = 0.225$, $b_f/L = 0.250$, $b_f/L = 0.275$, $b_f/L = 0.300$, $b_f/L = 0.325$, $b_f/L = 0.350$, $b_f/L = 0.375$, $b_f/L = 0.400$

FIGURE 3. Time series of the normalized pressure at Rijke tube inlet for flame locations varying from $b_f/L = 0.1$ to $b_f/L = 0.4$

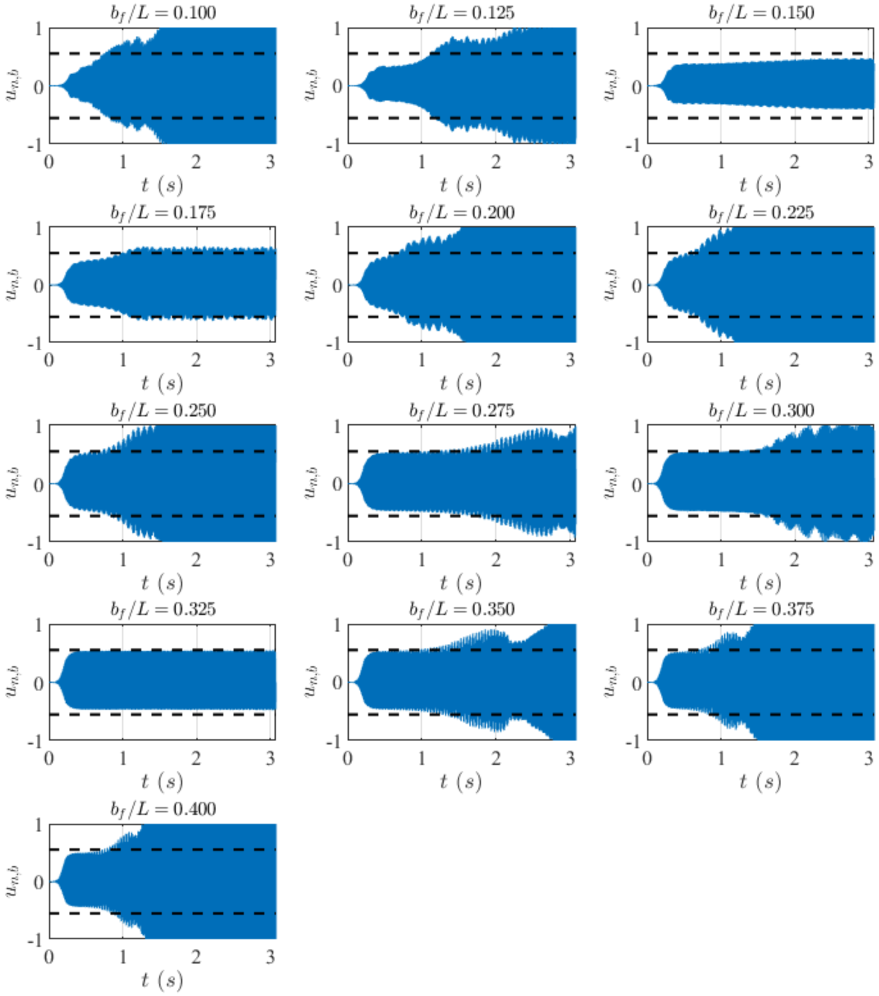

Figure 4. Time series of the normalized velocity at location right upstream of the flame for flame locations varying from $b_f/L = 0.1$ to $b_f/L = 0.4$

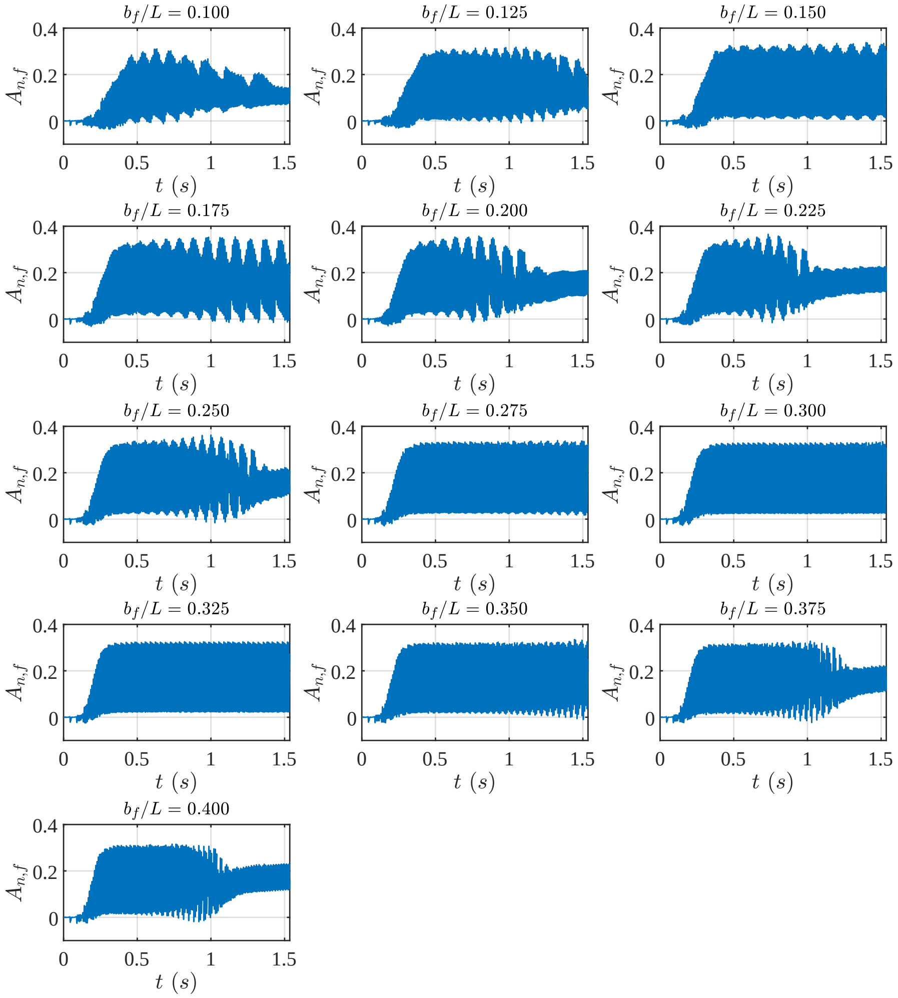

FIGURE 5. Time series of the normalized flame area for flame locations varying from $b_f/L = 0.1$ to $b_f/L = 0.4$

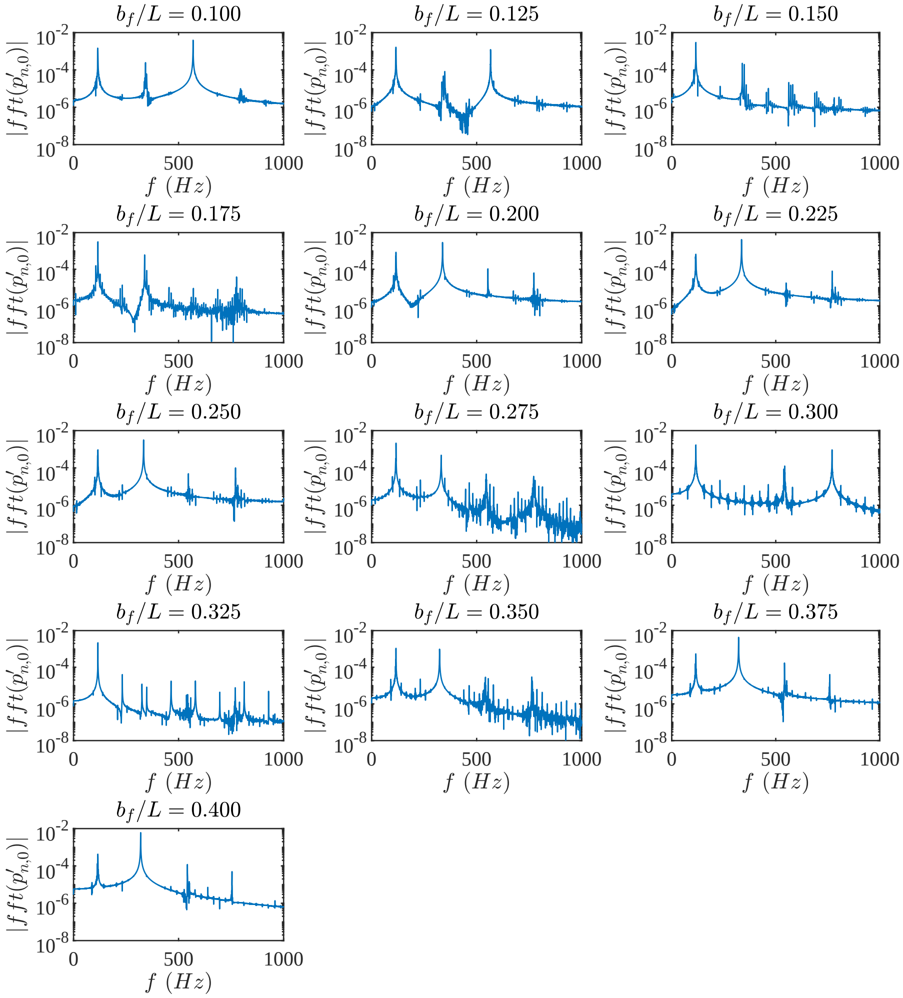

Figure 6. Spectra of the normalized pressure at Rijke tube inlet for flame locations varying from $b_f/L = 0.1$ to $b_f/L = 0.4$

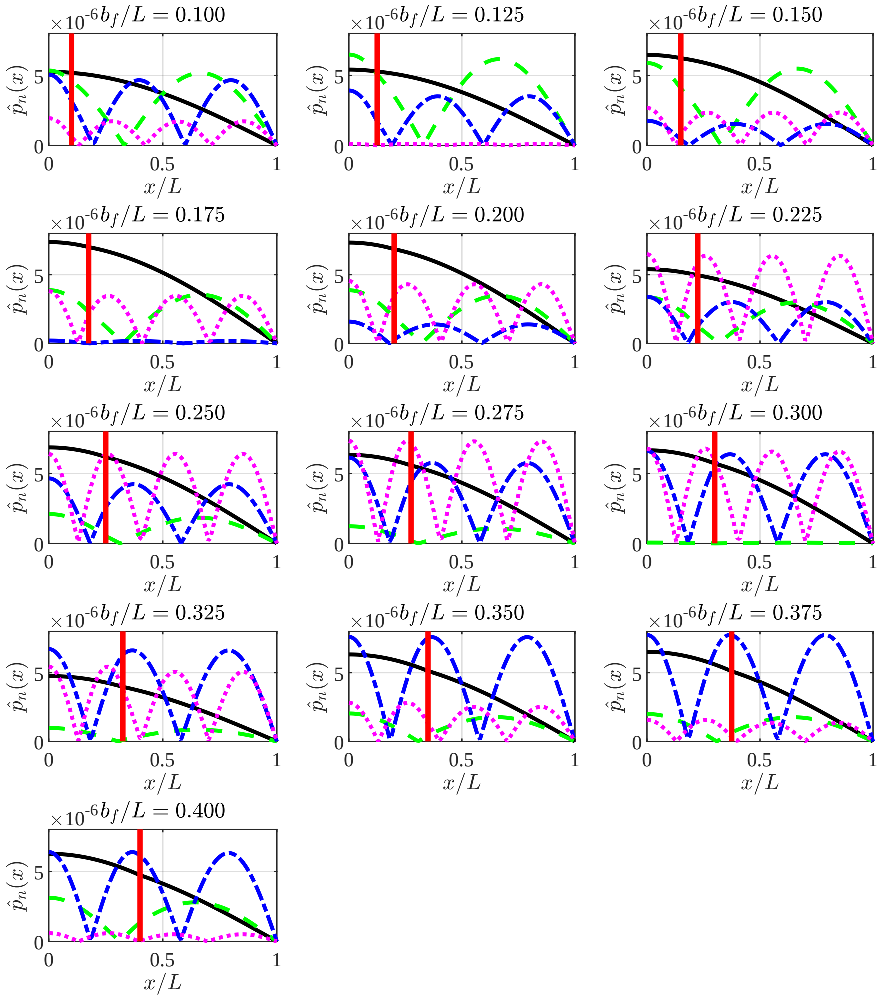

FIGURE 7. Acoustic mode shape of the normalized pressure oscillation along the Rijke tube for different flame locations: ——, 1^{st} mode; - - -, 2^{nd} mode; —·—, 3^{rd} mode; ·······, 4^{th} mode.

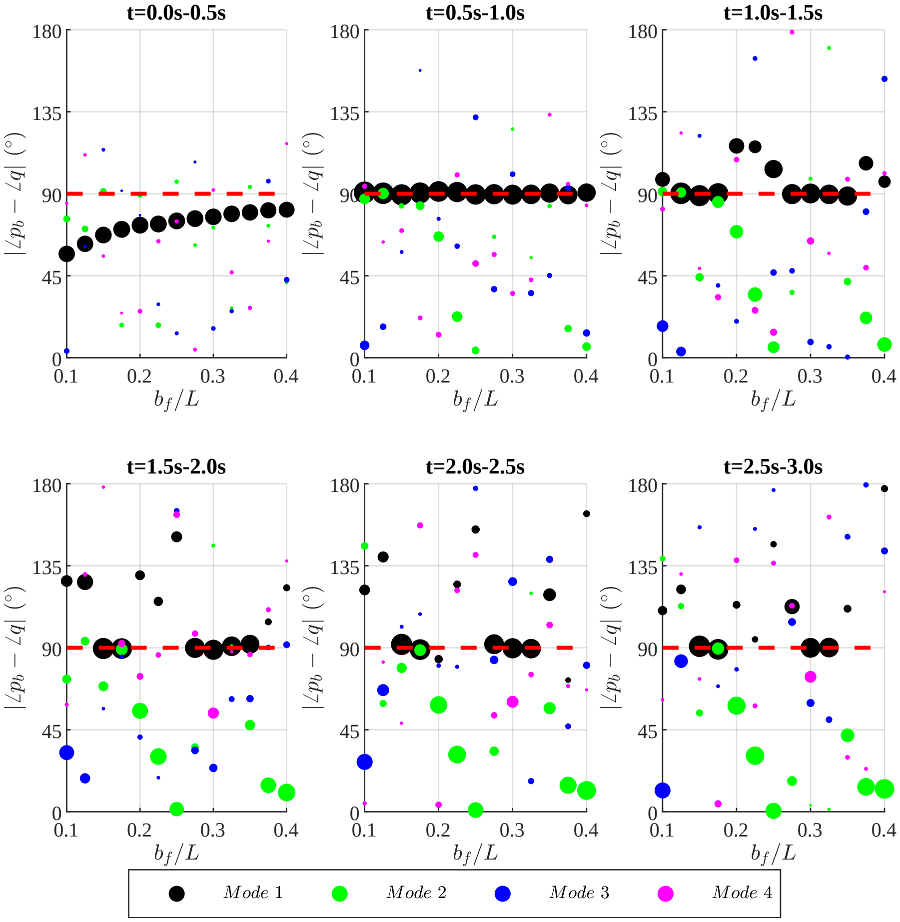

FIGURE 8. Phase difference between oscillations of pressure at flame location and flame area within three time durations for different flame locations

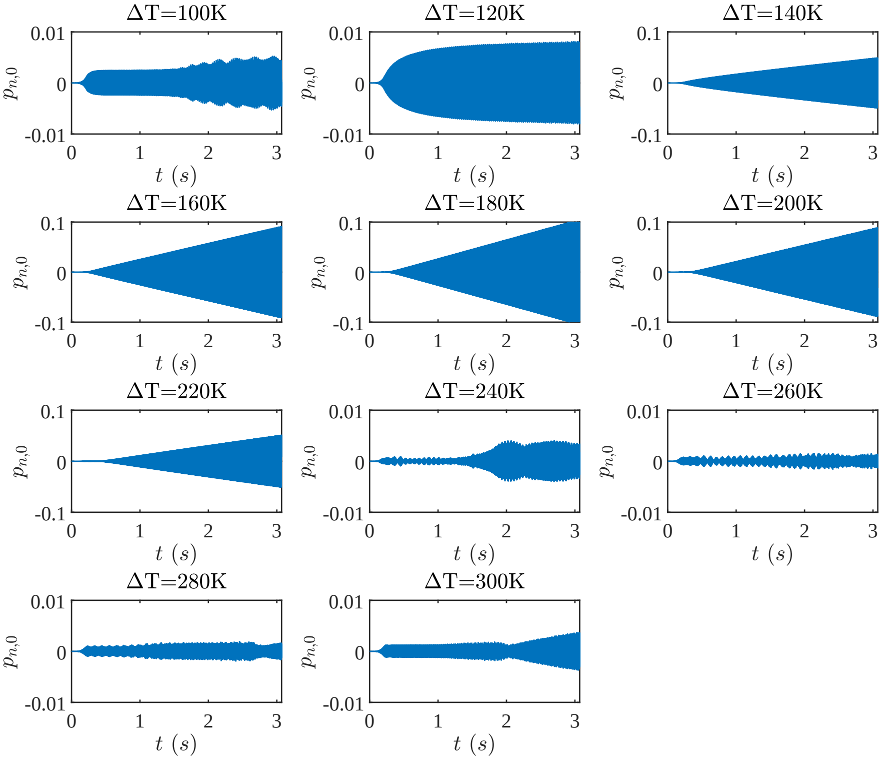

FIGURE 9. Time series of the normalized pressure at Rijke tube inlet for temperature rises varying from $\Delta T = 100K$ to $\Delta T = 300K$

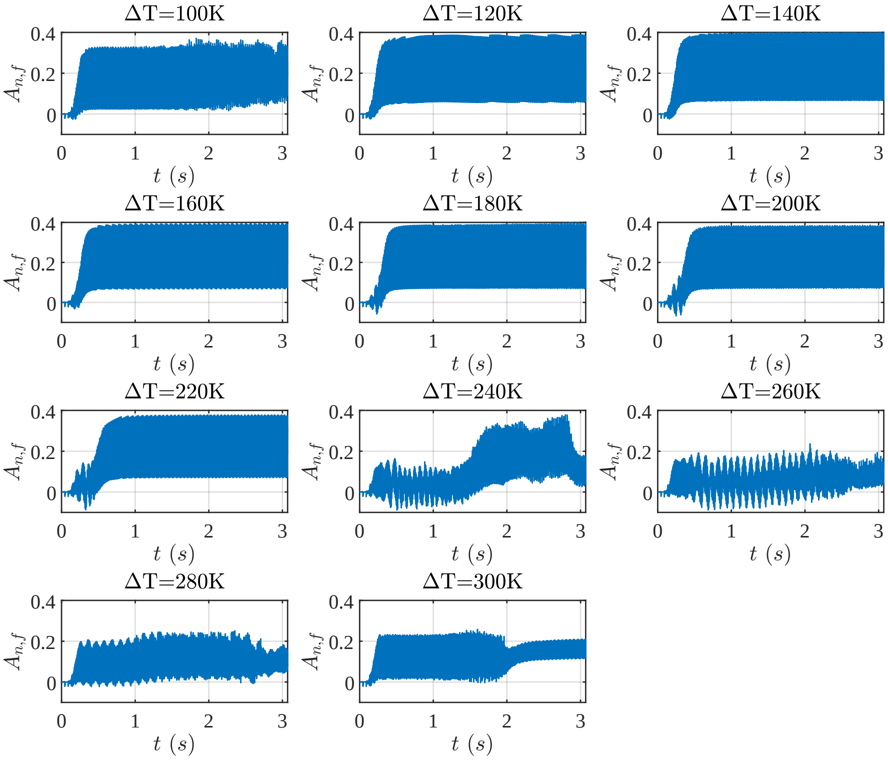

Figure 10. Time series of the normalized flame area oscillation for temperature rises varying from $\Delta T = 100K$ to $\Delta T = 300K$

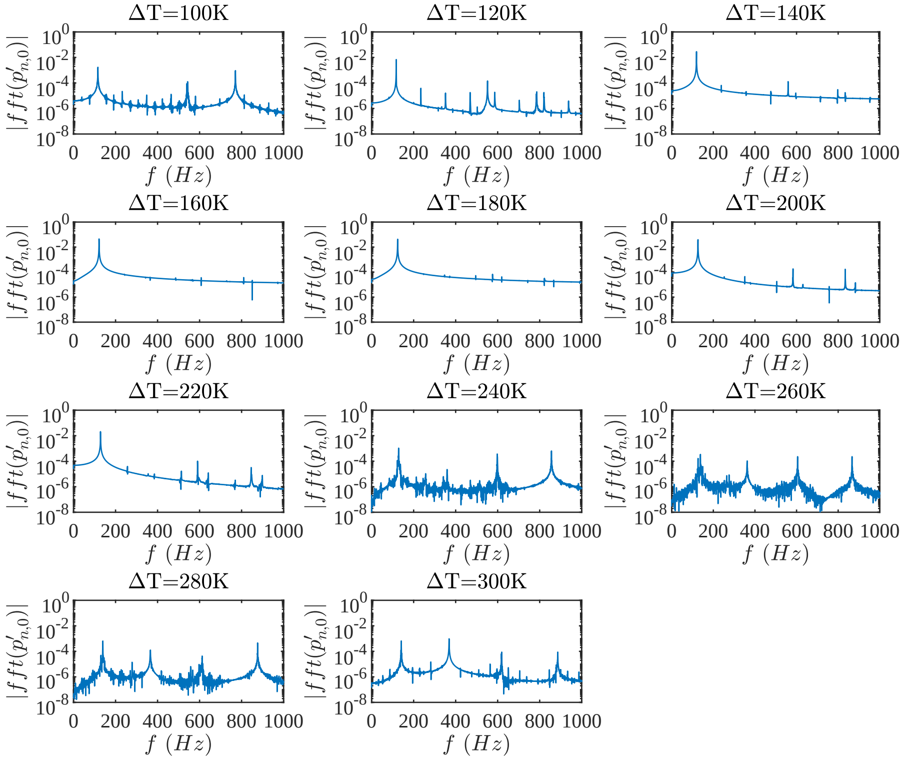

FIGURE 11. Spectra of the normalized pressure at Rijke tube inlet for temperature rises varying from $\Delta T = 100K$ to $\Delta T = 300K$

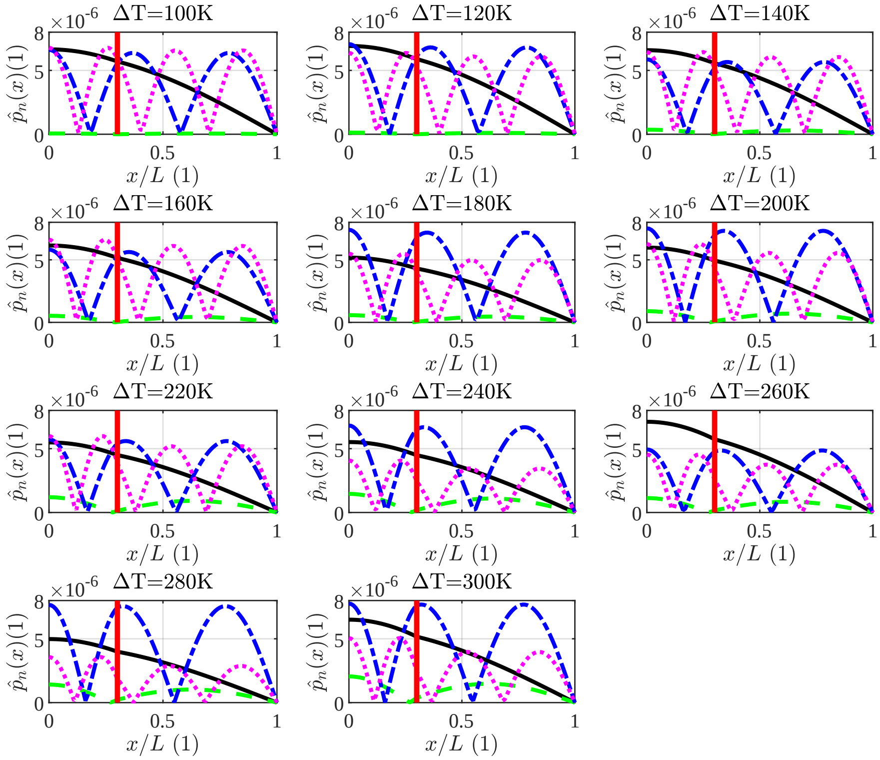

FIGURE 12. Acoustic mode shape of the normalized pressure oscillation along the Rijke tube for different temperature rises: ——, 1^{st} mode; - - -, 2^{nd} mode; —·—, 3^{rd} mode; ⋯⋯, 4^{th} mode.

The mode shapes for the first four dominant acoustic mode of the pressure oscillation are in Fig. 12.

The phase difference between the oscillations of pressure at flame location and flame area is summarized in Fig. 13.

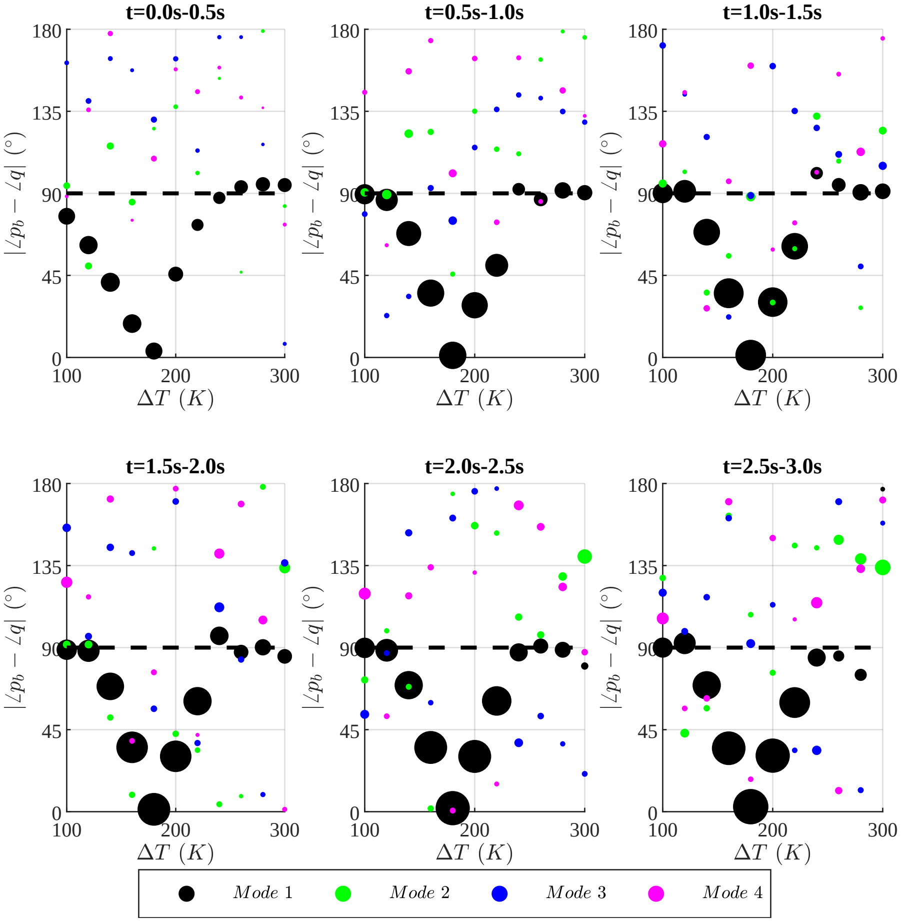

FIGURE 13. Phase difference between oscillations of pressure at flame location and flame area within three time durations for different temperature rises